Near Surface Geophysics, 2013, **11**, 307-316 doi:10.3997/1873-0604.2012067

2D elastic full-waveform imaging of the near-surface: application to synthetic and physical modelling data sets

François Bretaudeau[1], Romain Brossier[2], Donatienne Leparoux[1], Odile Abraham[1] and Jean Virieux[2]

[1] *Institut Francais des Sciences et Technologies des Transports, de l'Aménagement et des Réseaux (IFSTTAR), Nantes, France*
[2] *Institut des Sciences de la Terre, Université Joseph Fourier (ISTerre), Grenoble, France*

Received March 2011, revision accepted December 2012

ABSTRACT

Standard seismic methods are generally not well adapted to provide sharp quantitative images of the first few metres of underground. A two-dimensional full-waveform inversion of land seismic data, based on frequency-domain viscoelastic modelling, offers a promising approach to take advantage of the full complexity of seismograms and to simultaneously build 2D images of V_P and V_S parameters. In order to understand the behaviour of this method in a near-surface context and anticipate the corresponding field applications, we perform this investigation by applying waveform inversion on a simple layered medium. We first use synthetic data obtained from numerical modelling and then we employ laboratory data obtained by small-scale physical modelling. We demonstrate that such a near-surface 2D model can be quantitatively determined even in a realistic situation where the data are dominated by high-amplitude surface waves. A comparison of results derived for the same medium from ideal synthetic data and noisy experimental data allows detecting anomalies in the reconstruction of velocity models due to the experimental nature of the data used.

INTRODUCTION

Quantitative imaging of the first few meters of underground, in either 2D or in 3D, with seismic methods constitutes a key challenge for various applications, such as soil characterization in geotechnics, landscape management, risk analysis, environmental analyses and archaeology. However, high heterogeneity and strong seismic attenuation in the near-surface typically causes the seismic data to be dominated by energetic and complex surface waves. Given that refracted and reflected body waves are sometimes difficult to identify in such contexts, near-surface heterogeneities can prove difficult to image using tomography or migration of surface seismic data. Moreover, the dispersion analysis of surface waves (MASW) is not efficient in the presence of strong lateral variations or when there are very complex structures and it remains a low-resolution imaging approach.

Full-waveform imaging methods, developed in the time domain (Tarantola 1984) as well as in the frequency domain (Pratt 1999), are currently the subject of intensive research in the field of oil prospecting and, more generally, in crustal imaging. However, these methods have hardly been investigated in near-surface applications (Gélis *et al*. 2007). Full-waveform inversion (FWI) with the elastic approximation could help benefit from the full complexity of the near-surface seismic data by taking into account not only the reflected, refracted and surface waves but also all near-surface diffractions of P-, S- and surface waves.

Full-waveform inversion has been successfully applied on field data with the acoustic approximation for deep imaging (Operto *et al*. 2004), for cross-hole measurements (Pratt and Shipp 1999) and for near-surface exploration using the refracted wavefront (Gao *et al*. 2007). But it was only recently tested with the elastic approximation on synthetic data (Gélis *et al*. 2007; Romdhane *et al*. 2009; Bretaudeau 2010) and still remains difficult. Application of such a new imaging method directly on field data at this scale would be difficult, especially because of the many uncontrolled parameters in field measurements, like coupling of sources and receivers, mechanism of the excitation, poor *a priori* information, strong attenuation, strong measurement noise, etc. Before applying this method to field data, it is necessary to evaluate: a) how the imaging technique behaves in the near-surface context; and b) how the method performs on noisy experimental data. It is also important to define what can occur when applying a FWI algorithm to experimental data that cannot fully be explained by forward modelling. With this goal, we present here a simple 2D case. Through a combined approach involving numerical simulation and small-scale physical modelling, we investigate how elastic waveform inversion in the frequency domain can lead to a quantitative reconstruction of near-surface heterogeneities. We chose a configuration in which such

© 2013 European Association of Geoscientists & Engineers

reconstruction is difficult since layer interfaces are too deep and the impedance contrasts too weak to generate refracted waves or dispersive surface waves in the data. In addition, reflected body waves are mainly hidden by the surface waves in the data, thus making the migration process inefficient. The imaging experiment presented here involves synthetic data generated by a viscoelastic discontinuous Galerkin finite-element modelling algorithm (Brossier *et al*. 2008), as well as experimental data obtained for a similar medium through a small-scale modelling experiment with a laser ultrasonic device dedicated for seismic data acquisition (Bretaudeau 2010; Bretaudeau *et al*. 2011). First, we show how to generate the synthetics and obtain similar experimental data, which are then examined and compared. Next we present the results of elastic waveform inversion on both synthetic data and experimental ultrasonic data using the waveform inversion algorithm developed by Brossier (2010). These results are finally analysed and quantitative images derived from synthetic data and laboratory experimental data are compared.

METHODOLOGY

Model building

In this study we use a combined approach involving a numerical medium and a small-scale experimental medium, the two being similar to each other. The 2D numerical medium shown in Fig. 1 was built using the dimensions and viscoelastic properties of the epoxy-resin physical model presented in Fig. 2. These properties were determined by means of independent ultrasonic measurements. Both the physical and synthetic media are composed of three layers with velocities increasing with depth, V_P from 2300–2740 m.s^{-1} and V_S from 1080–1427 m.s^{-1}. Quality factors Q_P and Q_S and bulk densities are also estimated. The dimensions and viscoelastic properties of the model are presented in the first column of Table 1. The upper layer is 35 mm thick and contains a high-velocity elliptical inclusion (properties similar to those of the deepest layer). The intermediate layer is 5 mm thick. The deepest layer simulates the underlying semi-infinite half-space. The physical model was built by casting small layers of epoxy resin from the bottom to the top of the model sequentially before complete polymerization of the latter layer. This procedure ensures a good contact between the layers, avoids the presence of small bubbles and reduces strong deformations due to exothermic polymerization of the epoxy resin. The physical model is large enough (L = 500 mm, l = 400 mm, h = 260 mm) to simplify elimination of the boundary effects and simulate a semi-infinite medium. The numerical medium shown in Fig. 1 is built with the dimensions of 180 mm in length and 50 mm in depth. This small area corresponds to the investigated part of the small-scale medium. The numerical model is limited on the top by a free surface and is bound on the three other sides by PML (Perfectly Matched) layers (Berenger 1994) to avoid undesirable edge reflections. The source signal is a 100 kHz Ricker wavelet.

As an example, these physical and numerical models are able to simulate the near-surface with a scale factor of 1:2 for velocities, 1:2000 for frequencies and 1:1000 for distances. The model is meant to simulate a full-scale medium 180 m long and 50 m deep, with P-wave velocities ranging between 1150–1400 m.s^{-1} and S-waves between 540–713 m.s^{-1}, with an inclusion located at a depth of 15 m. The data spectrum would thus be centred at 50 Hz. Table 1 provides more details about the properties and dimensions of the large-scale experiment that corresponds to the small-scale model for these scale ratios. The quality factor Q is a dimensionless coefficient that describes the loss of energy per cycle and hence scaling is not needed. The scale ratio for density has no importance because density only affects the amplitudes of waves through reflection and transmission coefficients that are defined as impedance ratios ($R = (Z_1 - Z_2) / (Z_1 + Z_2)$ and $T = 1 - R$ with Z_1 and Z_2 being the acoustic impedances in the two layers). Thus an arbitrary but constant scaling is applied to the density. Note that the impedance contrasts between the various materials here are rather weak and lead to reflection coefficients less than 0.13.

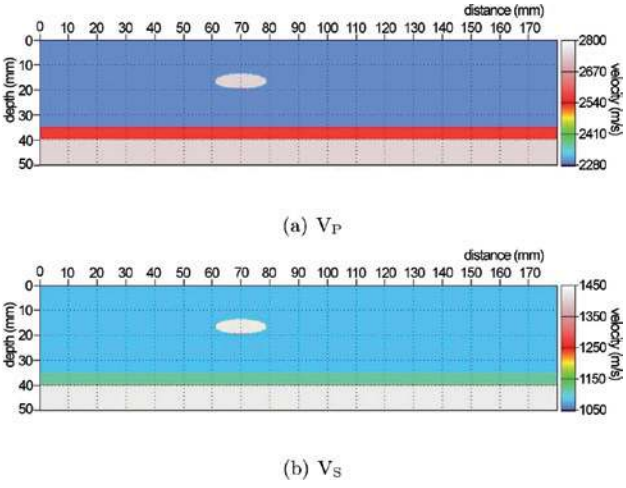

FIGURE 1
The exact V_P and V_S velocity models.

Ultrasonic data generation

The same acquisition survey is used for both the numerical and the physical model. It is composed of 37 source points and 180 receiver points that are distributed regularly all along the free surface with increments of 5 mm and 1 mm, respectively. The smallest source-receiver distance is 10 mm. The ultrasonic data

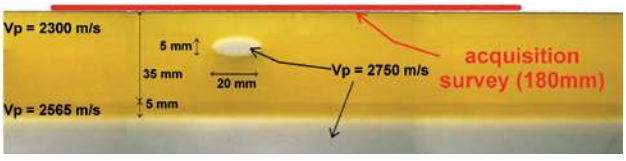

FIGURE 2
Cross-section of the three-layer epoxy resin model: low-velocity layer in yellow, 5 mm intermediate layer in orange, fastest material in white. The red line indicates the measurement profile, which corresponds to the width of the synthetic model (Fig. 1).

Scale	**Model scale**			**Field scale example**			**scale ratio**
Material	(1)	(2)	(3)	(1)	(2)	(3)	
V_p (m/s)	2 300	2 565	2 740	1 150	1 282	1 370	1:2
V_s (m/s)	1 080	1 118	1 427	540	559	713	1:2
ρ (kg/m^3)	1 465	1 195	1 601	1 465	1 195	1 601	1
Q_P	55	65	85	55	65	85	1
Q_S	22	26	34	22	26	34	1
f_{min}		30 kHz			15 Hz		1:2 000
f_0		100 kHz			50 Hz		1:2 000
f_{max}		250 kHz			125 Hz		1:2 000
Profile length		180 mm			180 m		1:1 000
Investated depth		50 mm			50 m		1:1 000
dx shots		5 mm			5 m		1:1 000
dx geophones		1 mm			1 m		1:1 000
Inclusion size		18 mm			18 m		1:1 000
Inclusion depth		15 mm			15 m		1:1 000
Position accuracy		10 μm			10 mm		1:1 000
Particle displacement at the source location		50 μm			50 mm		1:1 000

TABLE 1

Table showing material properties in the physical model and a corresponding field seismic experiment: viscoelastic parameters for the three different material types, frequencies and dimensions.

set is obtained with the recently developed MUSC laser-ultrasonic measurement bench (MUSC being the French acronym for Non-Contact Ultrasonic Measurement) recently developed by Bretaudeau (2010) and Bretaudeau *et al*. (2011). The MUSC bench was designed to simulate seismic experiments at different scales, with both the parametric control and the great accuracy allowed by laboratory conditions, in order to assess innovative imaging techniques and calibrate measurements for the purpose of preparing large-scale experiments. The viscoelastic properties of the samples are well controlled by means of independent ultrasonic measurements. The geometry of the model is also controlled by means of high-frequency (5 MHz) ultrasonic measurement. The vertical particle displacement is recorded by a Bossa Nova TEMPO laser interferometer (Bossa Nova Technologies 2010) with the capacity to record real amplitudes of particle displacement without any disturbances and uncertainties caused by coupling. Several types of piezoelectric sources make it possible to generate an ultrasonic excitation over various frequency ranges from 10 kHz to 5 MHz and to introduce a spatially extended or point excitation. In our configuration, the MUSC bench provides a multi-source and multi-receiver surface seismic data set. The ultrasonic point source is excited by a 100 kHz Ricker wavelet. The contact size of the piezoelectric source that we used is sufficiently small (1 mm) compared to the wavelengths and hence provides the typical omnidirectional radiation pattern expected for the seismic sources. Such a piezoelectric contact source generates a force normal to the surface. This mechanism corresponds to a compressional hammer-impact or a vibrating source. The data are sampled at 10 MHz (dt = 0.1μs) and the record length is 1.0 ms. Each signal is stacked and averaged on-the-fly 512 times. The source and

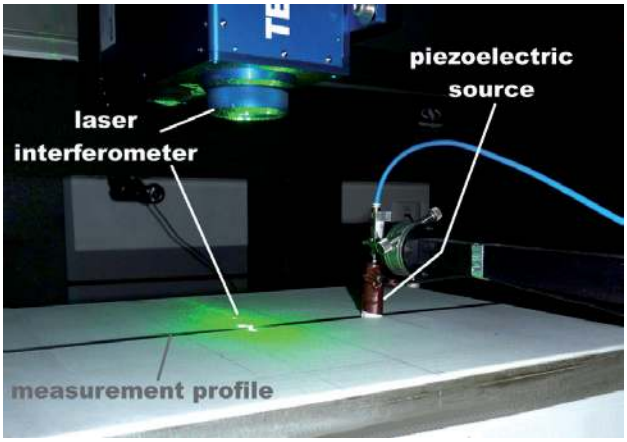

Figure 3

Laser-ultrasonic acquisition of seismic data in the small-scale model by the MUSC laboratory system. The piezoelectric source is pressed at the model surface with a constant force. The BOSSA-NOVA interferometer records the vertical particle displacement at a surface point. Both the source and receiver are moved sequentially over the measurement profile.

receiver points are sequentially moved automatically over the profile line. The source and receiver position have an accuracy of 10μm. This high accuracy is essential to ensure good reproducibility of measurements. Figure 3 illustrates the acquisition of seismic data along a seismic line, as performed at the MUSC laboratory. With 24 seconds to record a signal at each measurement point, the whole ultrasonic data set with 37 shot positions and 180 receiver points was acquired in 44 hours.

NUMERICAL AND SMALL-SCALE EXPERIMENTAL SEISMIC DATA

Experimental data

Two raw ultrasonic shot gathers corresponding to shot positions 1 (x = 0) and 37 (x = 180) are presented in Fig. 4. On both we can identify the direct P-wave, the Rayleigh wave and P- and S-reflected waves at layer boundaries. Several undesired effects are also recorded: the air wave propagating along the surface at 340 m/s, various hyperbolas corresponding to body and Rayleigh wave reflections at the boundaries of the model and disturbances generated by the power amplifier used for the ultrasonic source. Events 4–6 are considered as noise and have to be removed before processing the data. In this example, the preprocessing step included band-pass filtering to remove low- and high-frequency noise and a combination of f-k filtering and muting to remove the undesirable events 4–6. An empirical $\sqrt{t}$ factor is then applied to the entire data set in order to convert the 3D geometrical spreading of the body and surface waves into a 2D spreading. The $\sqrt{t}$ amplitude correction is valid only in the acoustic case for media that are spherically symmetric (Wapenaar *et al*. 1992) but Pratt (1999) showed that this correction is sufficiently accurate for 2D waveform inversion. The shot gather at position 1 after preprocessing is shown in Fig. 5(a). We can identify the direct P- and Rayleigh

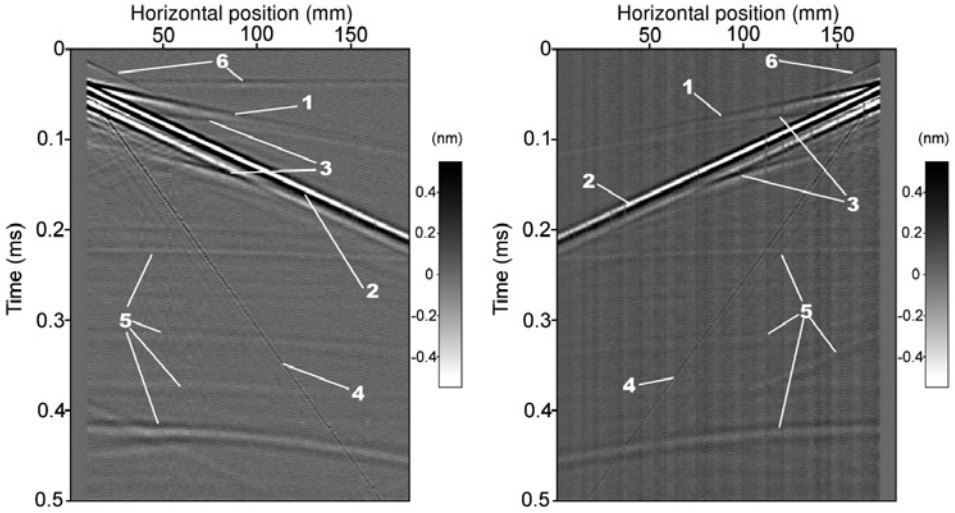

(a) Raw shot gather 1 (x = 0 mm) (b) Raw shot gather 37 (x = 180 mm)

FIGURE 4
Ultrasonic raw shot gathers from the extreme left and the extreme right of the measurement profile (x = 0 mm and x = 180 mm). The numbers marked here are: 1) direct P-wave, 2) Rayleigh wave, 3) P- and S- reflections, 4) air wave, 5) body and surface wave reflections from the boundaries of the model, 6) disturbances generated by the power amplifier used for the ultrasonic source.

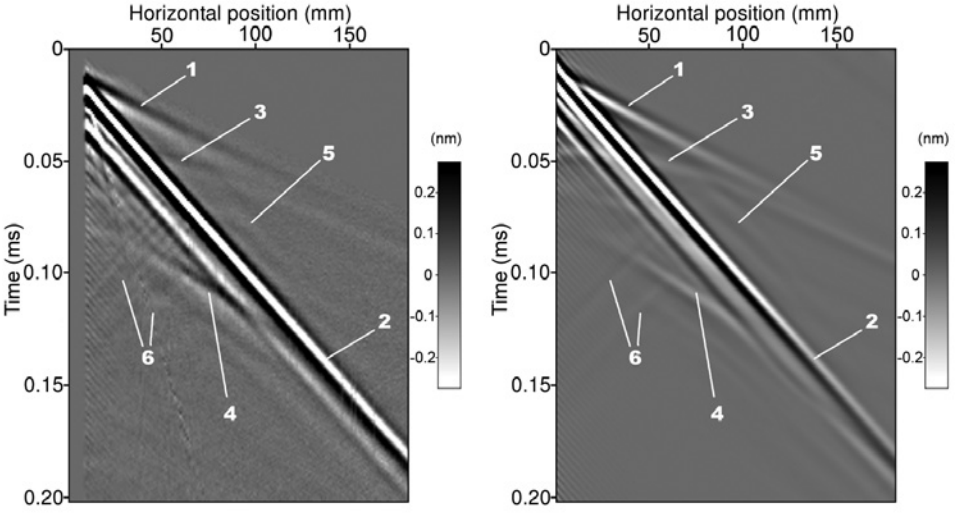

(a) Ultrasonic shot gather from position 1 (x = 0 mm) (b) Synthetic shot gather from position 1 (x = 0 mm).

FIGURE 5
(a) Ultrasonic shot gather after preprocessing and (b) corresponding synthetic shot gather (shot position 1). The events marked are as follows: 1) direct P-wave, 2) Rayleigh wave, 3) and 4) P- and S- reflections, 5) P-wave diffraction by the inclusion, 6) Rayleigh wave diffraction. All events observed in the ultrasonic data were reproduced in numerical modelling. The arrival times and amplitudes are both respected.

waves, very weak P- and S-reflected waves at the deep layer boundaries, a very weak P-wave diffraction and a Rayleigh wave diffraction. Events 5 and 6 in Fig. 5(a) are associated with the rigid elliptical inclusion located between $x = 60$ and $x = 80$ mm. Arrival times of reflected events are difficult to detect since they are partially hidden by the Rayleigh wave and because of the low-frequency content of the data. The second and third layers are too deep and the attenuation is too high to record the refracted waves. The phase velocity dispersion diagram calculated by the P – ω transform (Mokhtar *et al*. 1988) is presented in Fig. 6; it reveals that the deep layers are too deep to cause any surface wave dispersion for the frequency content of the data. In contrast, it is clear that the near-surface high-velocity inclusion generates body wave diffractions but above all a Rayleigh wave diffraction. However, it is difficult to compare these diffractions in a quantitative sense. All the information necessary to image the investigation domain are present in the data but it still remains difficult to treat each part of this wavefield separately by conventional methods in order to generate a high-resolution quantitative image of the medium.

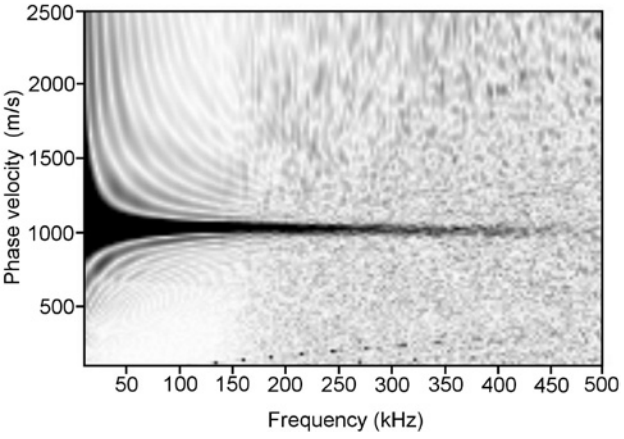

FIGURE 6

Phase velocity dispersion diagram extracted from a seismogram recorded far from the inclusion. The surface wave is non-dispersive over the frequency range 30–400 kHz.

Synthetic data

Synthetic data are calculated for the same source and receiver positions using the viscoelastic frequency-domain, discontinuous Galerkin finite-element modelling algorithm developed by Brossier (2010). The frequency domain allows describing and solving the propagation equations for each discrete frequency as a linear system:

$$\mathbf{AV} = \mathbf{S}, \tag{1}$$

where **A** is the impedance matrix containing the viscoelastic properties of the medium, **V** a vector containing the particle displacement in each cell of the finite-element grid and **S** a vector containing the source information. In this modelling approach, the free surface is implicitly modelled by the limits of the polygonal mesh grid. The semi-infinite size of the medium is assumed by PML layers (Berenger 1994). The source is modelled as a force normal to the free surface and is applied on a unique cell of the grid. Various techniques could be used to determine the source signature (see for instance Ghose 2002). In this work, the actual shape of the emitted source wavelet was estimated by linear optimization as proposed in Pratt (1999). The least-square norm of the mist between real and synthetic data calculated with the true medium is minimized by adjusting the phase and amplitude of the source wavelet for each discrete frequency. The 37 reconstructed wavelets from the 37 common shot gathers are displayed in Fig. 7(a) and their Fourier transform in Fig. 7(b). The extracted wavelets correspond to the frequency bandwidth (30–250 kHz) coupled with the time response of both the power amplifier and the piezoelectric source and the source coupling at each shot position. The shape of the 37 source wavelets is very similar. This illustrates the repeatability of the source excitation and the robustness of the wavelet inversion process. The temporal variations do not exceed 0.5 μs (8 times the period at $f_{max} = 250$ kHz). The error on amplitude reaches 5 dB at the two ends of the profile line (at shot numbers 1 and 37). Figure 8 depicts the evolution of the maximum amplitude of the source excitation along the measurement profile. It highlights spatial variations of the excitation, for example between 130–140 mm. These variations look small compared to possible amplitude variations in 'field data' but they must be considered carefully if we want to compare the experimental waveforms with computed ones and further apply waveform inversion.

Synthetic data can then be generated using these source wavelets and the same sampling parameters as those introduced for ultrasonic data. The common shot gather computed from the source position $x = 0$ mm is presented in Fig. 5(b) and may be compared with the ultrasonic shot gather of Fig. 5(a). P-wave, Rayleigh wave and body wave reflections, diffractions and Rayleigh wave disturbances generated by the rigid inclusion are all well reproduced, respecting both time arrivals and amplitudes. Figure 9 shows the comparison of experimental and computed signals extracted from the shot gathers of Fig. 5(a,b) for two source-to-receiver offsets $x = 20$ mm and $x = 60$ mm. As observed with source wavelet inversion, the phases of the signals are accurately reproduced but the error in amplitude can reach 8 dB for some frequencies. The remaining differences between the synthetic and ultrasonic data are mainly due to the presence of noise and the imperfect 3D-to-2D amplitude correction. It is well-known from experience that velocity imaging with waveform inversion is much more sensitive to phases than to amplitudes (Crase 1989; Pratt 1999; Shin and Min 2006; Kamei and Pratt 2008). Because in field experiments an error in amplitude will be difficult to avoid, we consider the misfit in the amplitude of our ultrasonic data to be acceptable. Both data sets can therefore be utilized in the same FWI. The differences between the results will point to imaging anomalies or discrepancies due to experimentation.

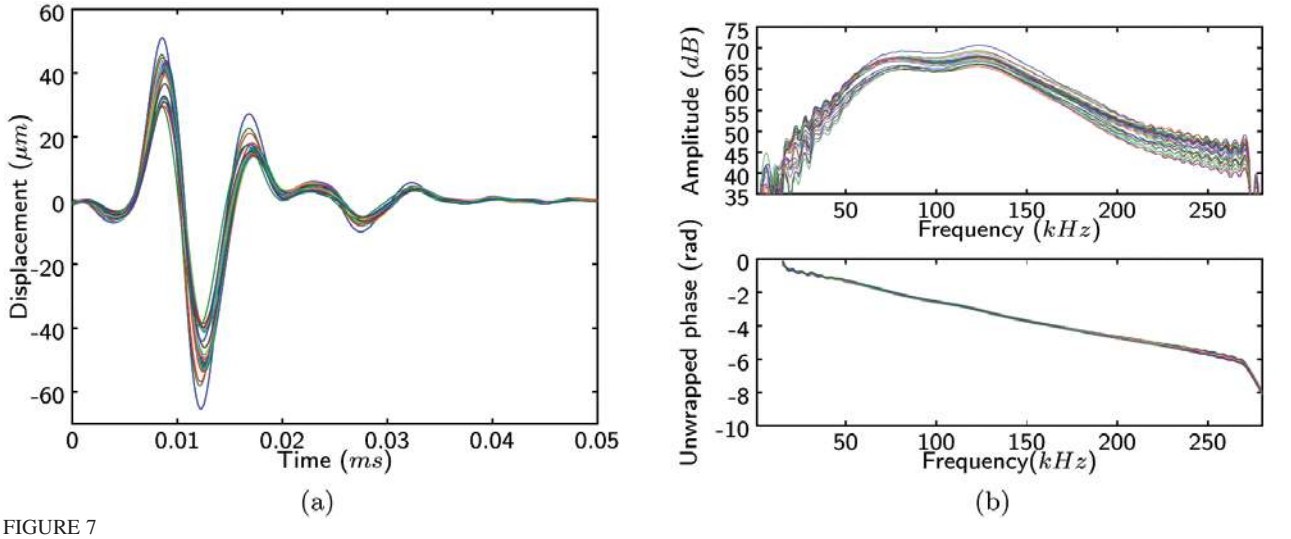

FIGURE 7

Source wavelets at the 37 point source locations, reconstructed by waveform optimization: (a) time-domain signal, (b) amplitude and phase spectrums. The time differences between the various wavelets do not exceed 0.5 μs and maximum 5 dB in amplitude. The extremes correspond to the shots at the two extremes of the profile.

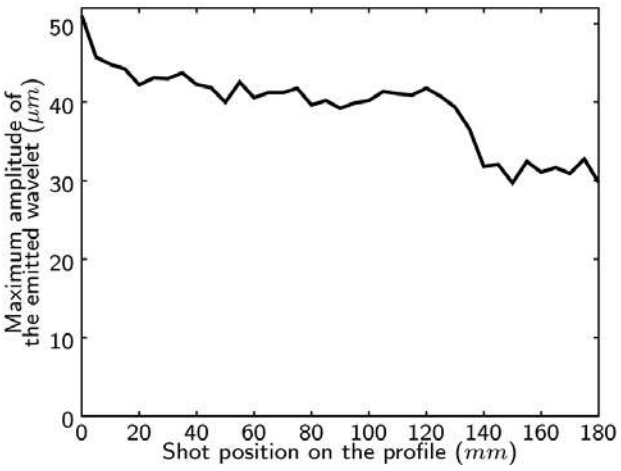

FIGURE 8

Maximum amplitude of the reconstructed source wavelets for the 37 shots. Although the phase of the emitted signal is very repeatable, amplitude changes are observed along the profile. Maximum amplitude dropped by 25% between shot positions at 120 mm and 140 mm.

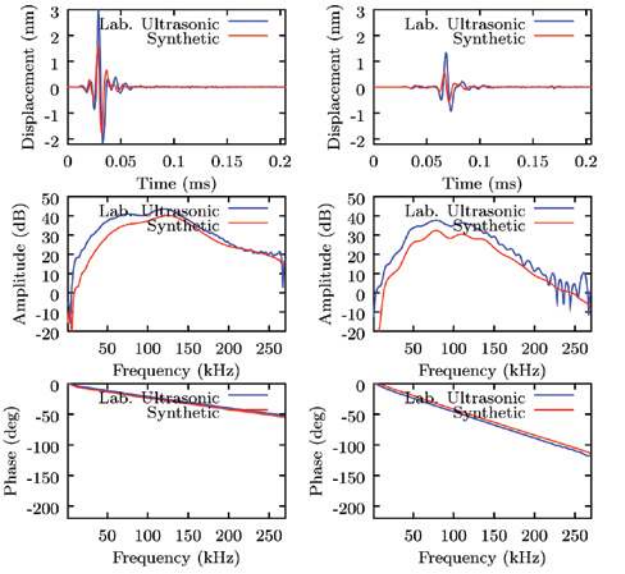

FIGURE 9

Comparison of experimental signals at two source-receiver offsets with those computed by numerical modelling. Signals were extracted from the shot gathers of Fig. 5 (shot location 1). Laboratory experiment and synthetic data are in good agreement. The phase of the signal is reproduced very accurately. Amplitude is reproduced with a maximum error of 8 dB at certain frequencies.

WAVEFORM INVERSION RESULTS

The waveform inversion strategy used here is based on the frequency-domain formulation proposed by Pratt and Worthington (1990). The algorithm we used (Brossier 2010) is based on iterative conjugate-gradient optimization. The forward solutions are computed in the frequency domain with the same finite-element code used to generate our synthetic data set. The pseudo-Hessian (Shin *et al*. 2001) is computed at the first iteration of each frequency to precondition the gradient. Many authors (Pratt and Worthington 1990; Pratt 1999; Sirgue and Pratt 2004) have demonstrated that this non-linear inverse problem can be solved only if the initial model is realistic enough and if the non-linearity is mitigated by introducing sequential information from low to high frequencies. For deep onshore imaging, Brossier *et al*. (2009) recommended using complex-valued frequencies as a second hier-

archical level to reduce non-linearity by introducing gradually refracted waves, reflected waves and ultimately converted and surface waves. In our data, the various kinds of waves are not sufficiently separated in time to be separated by complex frequencies. A range of approaches have in fact been proposed for building an initial model (Virieux and Operto 2009). The problem of building an accurate initial model is of crucial importance for waveform inversion whatever the scale and remains an open question today. This complex topic obviously needs further studies and will not be discussed in this paper. We choose in this study to start from the initial model presented in Fig. 11(a,b), which corresponds to a smoothed version of the true medium without the inclusion in the first layer. Both V_P and V_S parameters are inverted simultaneously, while the density and quality factors Q_P and Q_S of the initial model are considered sufficiently accurate and are kept constant during iterations. Fourteen frequencies are sequentially inverted: [29 kHz, 34 kHz, 39 kHz, 44 kHz, 49 kHz, 54 kHz, 63 kHz, 73 kHz, 83 kHz, 93 kHz, 107 kHz, 122 kHz, 137 kHz, 156 kHz], with 5 iterations for each frequency. The corresponding Rayleigh wavelengths therefore range between 35–6.5 mm when the inclusion is located at a depth of between 15–20 mm, respectively. The maximum theoretical resolution for the maximum frequency equals: $\lambda_{P_{min}} / 2 = 7.4$ mm for V_P, and $\lambda_{S_{min}} = 3.5$mm for V_S.

Although the conjugate gradient allows very strong and fast convergence, 5 iterations appear to be not many to obtain sufficient convergence. In fact, the choice of the maximum number of iterations is not simple. In the case of synthetic data inversion, more iterations lead to better results. In the case of real noisy data, too many iterations result, in some cases, in convergence to a local minimum even though the cost function is still decreasing significantly. Therefore the correct number of iterations cannot be easily defined. We thus prefer an uncompleted reconstruction with a few iterations rather than a local minimum. The iterative process is thus stopped when the mist function decrease starts to slow down. Figure 10 shows the decrease of the cost function for the first 10 iterations for the synthetic and experimental data sets. Convergence is much slower with the experimental data. Five iterations are enough to ensure significant convergence.

Figure 11(c,d) depicts the final result obtained from the synthetic data at the last chosen frequency (156 kHz). The inclusion and the deep layers are well localized and quantitatively imaged, with an accuracy that decreases with depth. The resolution is approximately twice as good for V_S than for V_P. Artefacts and differences, in comparison with the exact model, are due to the unfavourable one-side illumination as well as the lack of very low (< 29 kHz) and very high (> 156 kHz) frequency information in the available data. In particular, the vertical oscillations observed in the images are due to the lack of low-vertical wavenumbers in the initial model that cannot be entirely reconstructed by the inversion because the starting frequency is too high.

This result can be considered as the best possible result in this configuration and can be compared with that obtained by employing the same strategy but on ultrasonic experimental data. At each frequency and each iteration, a source wavelet for each shot position was determined previous to the model estimation. For the source estimation, we assumed that the velocity, density and attenuation models are exact. (Pratt 1999) explained that the cross-hole configuration permits a good representation of the source wavelet, when the velocity model is a smoothed version of the true model. In our configuration, the source wavelet is mainly extracted from information contained in the direct and Rayleigh wave that propagate only in the first layer. Thus our initial velocity model can be considered to be sufficiently accurate to ensure a good source wavelet estimation. However, we are confident that the noise, the inaccurate attenuation model and the accumulation of error in the velocity model with iterations lead to errors in the source estimation. The final result obtained at the last frequency 156 kHz is depicted in Fig. 11(e,f). The inversion results obtained for the two data sets are close. However, the image obtained for the experimental data is disturbed with a lot of artefacts. The rigid inclusion is imaged similarly for both data sets and the deep layers are also detected, yet the magnitude of the estimated velocities is quite different. Also, the bottom of the model is not imaged correctly in V_S, a great number of inconsistent high-velocity heterogeneities appear in both V_P and V_S and we notice artefacts that systematically appear close to the positions of the sources. These artefacts are related to the imperfect source wavelet inversion and it possibly has an influence on imaging the rest of the model.

Looking at the representation of the spectral amplitude versus the offset of the data at six different frequencies for shot number 1 in Fig. 12, we find that the information at the lowest frequency (29 kHz) is very close to the noise level. Thus in a second step, we choose to start inversion from a higher frequency (34 kHz) and to freeze the first three millimetres of depth during the inver-

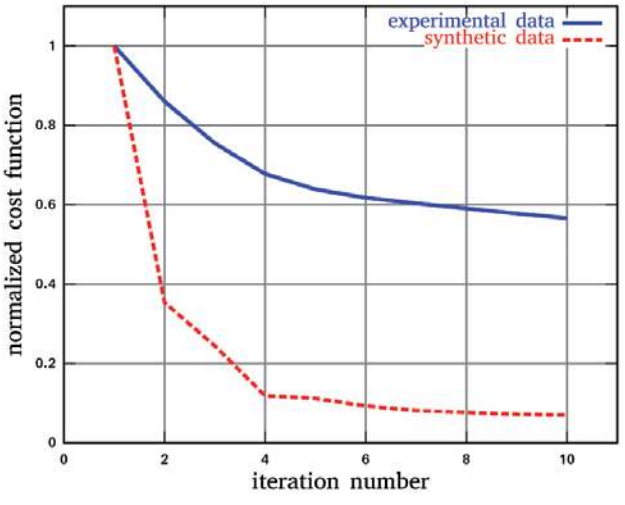

FIGURE 10
Normalized cost function at the first frequency for synthetic and experimental data sets. Convergence is slower for experimental data. Five iterations result in significant convergence.

sion in order to avoid any instabilities near the source points. However, a part of the frozen zone becomes slightly modified due to the smoothing of the gradient computed in the unfrozen zone. The 3 mm depth of freezing is chosen small, because the very near-surface is not supposed to be known but must be at least bigger than the correlation length of the Gaussian smoothing of the gradient.

The result is shown in Fig. 11(g,h). Due to the use of a first frequency that has a higher signal-to-noise ratio, the bottom of the model is now better recovered than when starting the inversion at 29 kHz. Freezing the upper part of the model removes the artefacts located close to the source and clearly reduces the inconsistent high-velocity heterogeneities that are present in all images. On the whole, this result shows a lot of similarities with the one obtained from synthetic data, yet several differences can be distinguished. For one thing, the differences in the magnitude of the velocities and in the size and location of the imaged structures can be attributed to the discrepancies between the physical and numerical models, as well as to a slower convergence on true velocities due to the presence of noise in the data. In particular, the representation of the frequency domain data in Fig. 12 illustrates how for this configuration, with high attenuation (Q_S = 22), the signal-to-noise ratio for some frequencies and for the largest offsets can be very low. Inversion

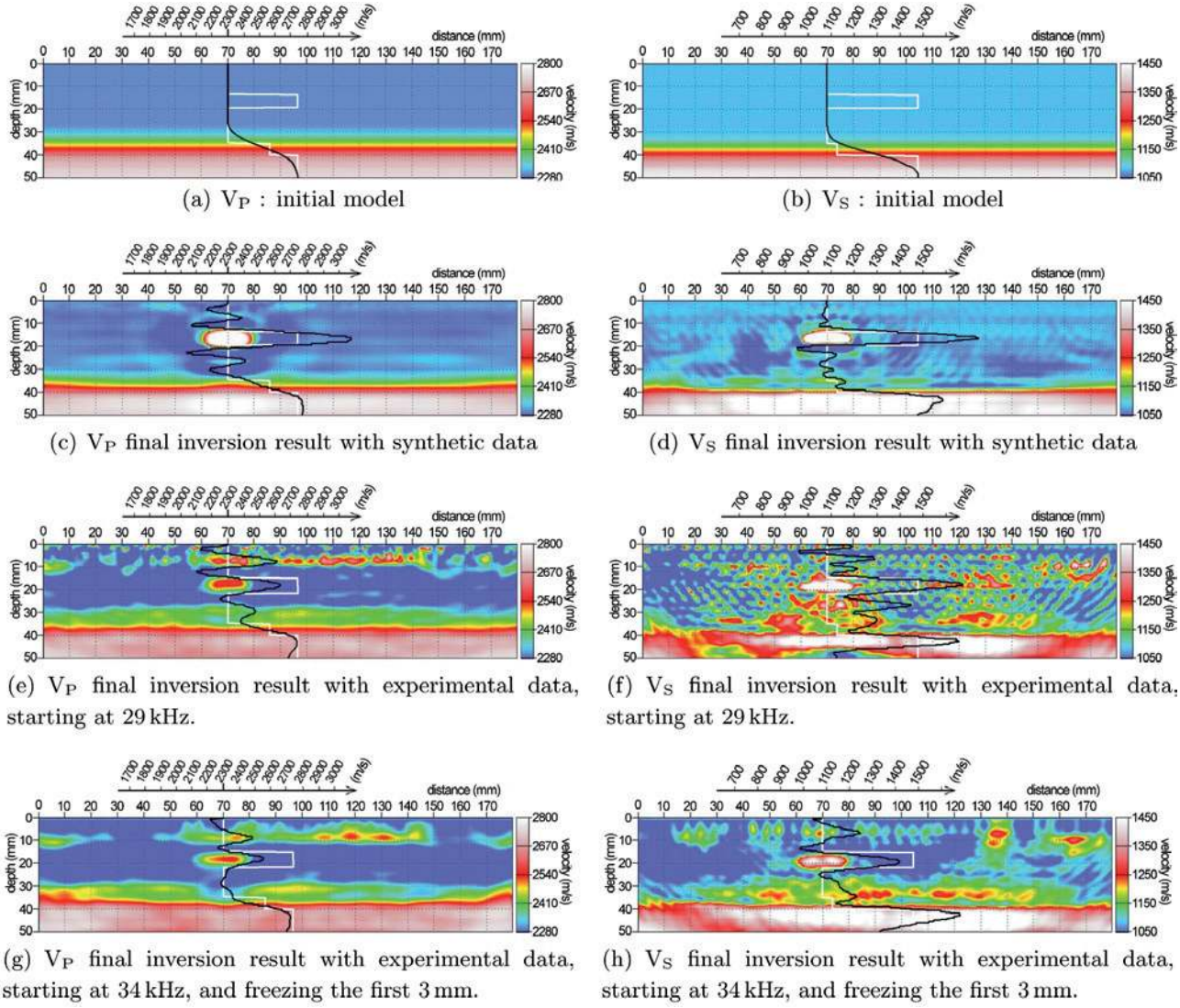

FIGURE 11

V_P and V_S velocity models obtained from sequential frequency-domain waveform inversion. (a) and (b) are the initial models and (c)–(h) are the final results obtained at 156 kHz respectively for synthetic data and for ultrasonic experimental data starting at 29 kHz and at 34 kHz and freezing the first 3 mm of depth. The theoretical imaging resolution is $\lambda P/2$ = 7.4 mm for V_P and $\lambda S/2$ = 3.5 mm for V_S. The black lines represent the vertical velocity profile passing through the centre of the inclusion. The white line provides the corresponding exact velocity profile as a reference.

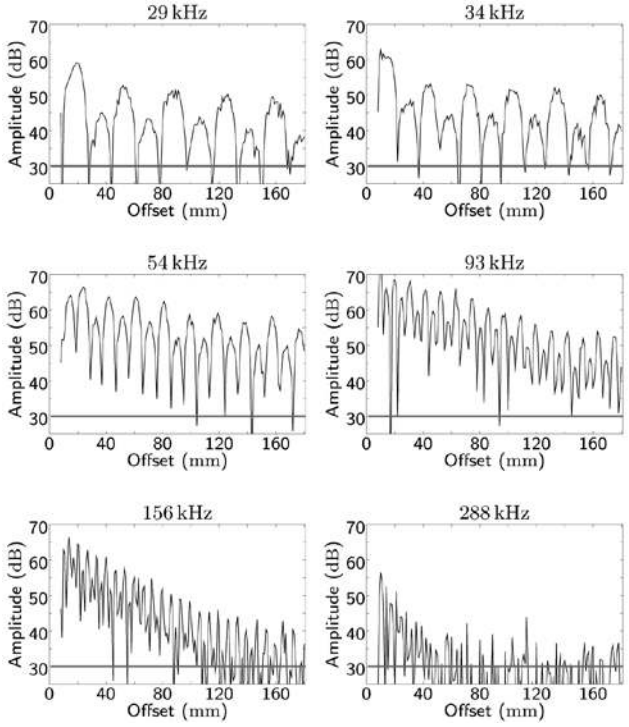

FIGURE 12

Fourier spectral amplitude versus offset for the traces in shot number 1 at six different frequencies: 29 kHz, 34 kHz, 54 kHz, 93 kHz, 156 kHz and 288 kHz. The horizontal line shows the background noise level. The observation of the amplitude of monochromatic wavefields with source-receiver distance gives a cyclic aspect to the curves. The curves lose their oscillating shape when the signal-to-noise ratio is too low or if the spatial sampling is too low (spatial aliasing).

is more unstable above 156 kHz since the data contain information only in near offsets, whereas noise is reserved for the large offsets. The signal-to-noise ratio versus both offset and frequency should, therefore, be a key parameter to be taken into account in optimizing the performance and stability in real data inversion.

We can also note in Fig. 11(g,h) that the artefacts mainly concentrated near the free surface (between 5–10 mm depth) are reduced when the upper part of the model is frozen but are still present in the images. These artefacts are correlated with higher non-linearity of the problem near the acquisition array where the computed gradient is singular, which in turn creates inversion instability when combined with data noise and mist. For instance, the high-velocity heterogeneity located between 130–140 mm at 10 mm depth in Fig. 11(h) correlates with the change in amplitude of source excitation at this position (see Fig. 8). Freezing the upper part of the model during the inversion process clearly helps reduce the influence of these artefacts. However, a better adjustment of this approach, coupled with better knowledge of the parameters in the uninverted zone and of source and receiver responses, would likely be necessary to control these instabilities.

CONCLUSIONS

A small-scale seismic experimentation on a laser-ultrasonic bench was performed to produce controlled seismic data. The experimental data were in good agreement with the numerical modelling. Such parametrization causes strong surface wave arrivals and weak diffractions. In this context, Full Waveform Inversion (FWI) in the frequency domain was applied following the strategy recommended by several authors. This approach consists, at first, in inverting the data for the lower frequencies and then introducing progressively higher frequencies in order to mitigate the non-linearity. We demonstrated on experimental data the potential of elastic FWI to quantitatively image complex near-surface structures, even in an unfavourable configuration with weak contrasts, strong attenuation and high-amplitude surface waves. The combined approach involving numerical simulation and small-scale experimentation has revealed imaging anomalies and discrepancies inherent to the experimental protocol including noise, uncertainty regarding source and receiver positions and inaccuracy of some parameters in the initial model. Results show that the observed artefacts are due not only to the strong non-linearity at very shallow depths, where surface waves dominate but also to the dependence of the signal-to-noise ratio on offset and frequency, to source signature inversion and to singularity of the gradient close to the sources.

The scaled physical experimental approach has allowed defining key issues, which will need to be treated in subsequent work on FWI of near-surface seismic data. Among others, the determination of the initial model and the dependence of the inversion results to the latter, accurate determination of the shallow layer to be frozen, preprocessing of the data and noise handling are key points that still need to be addressed before applying elastic FWI to near-surface field seismic data.

ACKNOWLEDGEMENTS

This study has been funded in part by the French research organizations ANR SEISCOPE and ACTENA and France's Pays de la Loire Regional Council. The authors would like to thank Stéphane Operto from Geoazur for all the fruitful discussions.

REFERENCES

Berenger J. 1994. A perfectly matched layer for absorption of electromagnetic waves. *Journal of Computational Physics* **114**, 185–200.

Bossa Nova Technologies. 2010. Bossa Nova website: http://www.bossa-novatech.com.

Bretaudeau F. 2010. *Modélisation physique à échelle réduite pour l'adaptation de l'inversion des formes d'ondes sismiques au génie civil et à la subsurface*. PhD thesis, University of Nantes.

Bretaudeau F., Leparoux D., Durand O. and Abraham O. 2011. Small-scale modeling of onshore seismic experiment: A tool to validate numerical modeling and seismic imaging methods. *Geophysics* **76**(5), T101-T112.

Brossier R. 2010. Two-dimensional frequency-domain visco-elastic full waveform inversion: Parallel algorithms, optimization and performance. *Computers and Geosciences* **37**, 444–455.

Brossier R., Operto S. and Virieux J. 2009. Seismic imaging of complex onshore structures by two-dimensional elastic frequency-domain full-waveform inversion. *Geophysics* **74**, WCC105–WCC118.

Brossier R., Virieux J. and Opertro S. 2008. Parsimonious infinite-volume frequency-domain method for (2-D) (P-SV)-wave modeling. *Geophysical Journal International* **175**, 541–559.

Crase E. 1989. *Robust elastic nonlinear inversion of seismic waveform data*. PhD thesis, University of Houston.

Gao F., Levander A., Pratt R., Zelt C. and Fradelizio G.-L. 2007. Waveform tomography to a ground-water contamination site: Surface reflection data. *Geophysics* **72**, G45–G55.

Gélis C., Virieux J. and Grandjean G. 2007. Two-dimensional elastic full waveform inversion using Born and Rytov formulations in the frequency domain. *Geophysical Journal International* **168**, 605–633.

Ghose R. 2002. High-frequency shear wave reflections from shallow subsoil layers using a vibrator source: Sweep cross-correlation versus deconvolution with groundforce derivative. 2002 SEG Annual Meeting in Salt Lake City, 1408–1411.

Kamei R. and Pratt R. 2008. *Waveform tomography strategies for imaging attenuation structure with cross-hole data*. Presented at the Proceedings of the 70th EAGE Conference and Exhibition in Rome.

Mokhtar T., Herrmann R. and Russel D. 1988. Seismic velocity and Q model for shallow structure of the Arabian shield from short period Rayleigh waves. *Geophysics* **53**, 1379–1387.

Operto S., Ravault C., Improta L, Virieux J. and Herrero A. 2004. Quantitative imaging of complex structures from dense wide-aperture seismic data by multiscale traveltime and waveform inversion: A case study. *Geophysical Prospecting* **52**, 625–651.

Pratt R. 1999. Seismic waveform inversion in the frequency domain, part 1: Theory and verification in a physical scale model. *Geophysics* **64**, 888–901.

Pratt R. and Shipp R. 1999. Seismic waveform inversion in the frequency domain, part 2: Fault delineation in sediments using crosshole data. *Geophysics* **64**, 902–914.

Pratt R. and Worthington M. 1990. Inverse theory applied to multi-source cross-hole tomography. In: Acoustic wave-equation method. *Geophysical Prospecting* **38**, 298–310.

Romdhane A., Grandjean G., Brossier R., Operto S. and Rejiba F. 2009. *Full waveform inversion of seismic data for 2D shallow structures imagery: Limitations and Perspectives*. Presented at the Proceedings of the 71st EAGE Conference and Exhibition 2009.

Shin C., Jang S. and Min D. 2001. Improved amplitude preservation for prestack depth migration by inverse scattering theory. *Geophysical Prospecting* **49**, 592–606.

Shin C. and Min D.-J. 2006. Waveform inversion using a logarithmic wave field. *Geophysics* **71**, R31–R42.

Sirgue L. and Pratt R. 2004. Efficient waveform inversion and imaging: A strategy for selecting temporal frequencies. *Geophysics* **69**, 231–248.

Tarantola A. 1984. Inversion of seismic reflection data in the acoustic approximation. *Geophysics* **49**(364), 1259–1266.

Virieux J. and Operto S. 2009. An overview of full-waveform inversion in exploration geophysics. *Geophysics* **74**, WCC1–WCC26.

Wapenaar K., Verschuur D. and Hermann P. 1992. Amplitude preprocessing of single and multicomponent seismic data. *Geophysics* **57**, 1178–1188.